# Preparation and characterization of activated CMK-1 with Zn and Ni species applied in hydrogen storage

Juliana M. Juárez, Marcos B. Gómez and Oscar A. Anunziata*,†

Centro de Investigación en Nanociencia y Nanotecnologia (NANOTEC), Facultad Regional Córdoba, Universidad Tecnológica Nacional, Maestro López y Cruz Roja Argentina, 5016, Córdoba, Argentina

## SUMMARY

The aim of this work is to prepare CMK-1 modified with Zn and Ni in order to improve its capacity in hydrogen storage. The approach that we have followed includes synthesis of nanostructures with the experimental study of its adsorption capacity and storage properties. We have shown that CMK-1 ordered porous carbon modified with metals is a promising material for hydrogen storage. The incorporation of metals was performed by wetness impregnation. The samples were characterized by X-ray diffraction, Fourier transform infrared spectroscopy, scanning electron microscope, transmission electron microscopy, X-ray photoelectron spectroscopy, and Brunauer–Emmett–Teller methods. The CMK-1 modified with Zn showed the highest $H_2$ uptake at 77 K and at low and high pressure (1.5 and 4.4 wt.% at 1 and 10 bar, respectively). The introduction of Ni into CMK-1 does not increase hydrogen storage capacity at low pressure. However, at a higher pressure (10 bars), Ni-CMK-1 displays improved results in hydrogen uptake compared with those of CMK-1 pristine, 2.4 and 2.1 wt.%, respectively. Copyright © 2015 John Wiley & Sons, Ltd.

**Correspondence**

* Oscar A. Anunziata, Centro de Investigación en Nanociencia y Nanotecnologia (NANOTEC), Facultad Regional Córdoba, Universidad Tecnológica Nacional, Maestro López y Cruz Roja Argentina, 5016, Córdoba, Argentina.
†E-mail: oanunziata@scdt.frc.utn.edu.ar

## 1. INTRODUCTION

Hydrogen is currently drawing considerable attention for its potential use as a clean fuel and other industrial applications [1] and has been shown to be able to successfully operate fuel cells and internal combustion engines [2], hence proving a viable alternative for nonrenewable energy sources such as oil. Automakers such as BMW, DaimlerChrysler, General Motors, and Ford successfully demonstrated the use of hydrogen as a fuel for the operation of some prototype cars [3].

The major challenge facing the hydrogen economy today is the development of a viable storage system for hydrogen, recognized as an ideal energy carrier for being clean and easily produced from renewable energy sources and for containing higher chemical energy per mass as compared with hydrocarbon fuels [4]. In the past decades, efficient hydrogen storage and transportation have been the major concern in hydrogen technology. The storage method leading to compressed hydrogen or liquefied hydrogen is difficult to use in some applications because of low storage density or high cost. Chemisorption of

hydrogen in the form of metals or complex hydrides is an interesting method, yet these materials are relatively expensive [4].

Many activated and templated carbons with high surface area exhibit potential for storing molecular hydrogen [4–7]. The activated carbons have been reported to have relatively high hydrogen storage capacity at 77 K [5,6]; however, pore size distribution is generally wide, and more than half of the total porous volume comes from macropores, contributing less to hydrogen uptake. Musyoka *et al*. demonstrated that there is great potential for the use of value-added clays to produce carbonaceous materials with more attractive properties for hydrogen storage applications [8]. S. N. Klyamkin *et al*. synthesized porous chromium (III) oxoterephthalate MIL-101 and hybrid MIL-101/Pt/C composite materials. The hydrogen adsorption properties of porous materials were investigated at pressures up to 1000 bar. Hydrogen sorption capacity increases gradually with pressure and reaches 1.5 wt.% compared with a maximum 0.4 wt.% for pristine MIL-101 [9]. Ren *et al*. conducted a review including the general requirements of metal–organic framework materials and

showed how these requirements can translate into desired characteristics such as the following: (i) structural stability; (ii) thermal conductivity; and (iii) hydrogen storage properties for further processing [10].

J. P. Singer et al. [11] reported hydrogen storage measurements on peels formed from powdered carbide-derived carbons mixed with polytetrafluoroethylene. E. Poirier et al. [12] studied hydrogen storage on carbon nanofibers (CNFs), intercalated and exfoliated carbon materials.

Nanostructured carbons are among the major candidates for physisorption because of their lightweight, abundant natural precursors, and low cost.

Carbon materials (especially in the form of tubes, fibers, and mechanically milled graphite) offer many advantages, such as low mass density and large surface area [13]. The hydrogen storage capacities are strongly influenced, not only by synthesis and purification conditions but also by the pretreatment of graphite nanofibers. The pretreatment creates edge dislocations and causes a spreading of adjacent layers in the crystal structure; these features can become regions for preferential hydrogen adsorption. It was found that hydrogen storage was fundamentally proportional to the specific surface area. Micropore diameter may thus play a key role in determining final storage capacity, implying that hydrogen-optimized pores can increase total hydrogen uptake [13]. Attempts to increase hydrogen uptake by graphite nanofibers have followed lines similar to those used in the case of carbon nanotubes. Metal hydride composites with graphite nanofibers, or even Pd, have been used [14]. Graphite nanofibers can be purified by removing amorphous carbon; caps over graphite layers can be removed to open up more planes for hydrogen adsorption. Further improvements can be sought for graphite nanofibers by carbon exfoliation via intercalation of high concentration acids followed by thermal shock, leading to a large increase of the surface area [14].

Carbon mesostructured from Korea (CMK) is one such family of ordered mesoporous carbons (MCs) [15]. Produced inside the channels of mesostructured silicates or aluminosilicates, CMK has specific surface areas ranging from 1000 to 2000 m$^2$/g and pore volumes from 0.5 to greater than 1 mL/g. These materials are promising for hydrogen storage applications. Porous carbons with well-ordered pore systems have offered great potential for hydrogen storage [16–19]. The carbons were obtained via the template method, involving the introduction of suitable carbon precursors to the ordered pores of the template, followed by carbonization and final template removal [20–22]. These carbon materials usually have large specific surface areas and high pore volume, useful for effective H$_2$ physisorption.

Ordered networks may also provide fast transportation in the materials; a noticeable volume of micropores can efficiently adsorb hydrogen, and microporosity and mesoporosity can be adjusted by changing the template, the carbon precursor, and the amount of carbon infiltrated in the template [16]. Moreover, carbon activation has also been reported to be useful for improving pore structure

and for increasing hydrogen uptake in new nanostructured carbon materials such as single-walled nanotubes [23] and CNFs [24]. Thus, activation of ordered porous carbon is desirable for yielding a higher hydrogen uptake. The amounts of hydrogen adsorbed at atmospheric pressure on single-walled nanotubes reach approximately 0.01 wt. % at 298 K and 1 wt.% at 77 K and H$_2$ sorption on CNF activated with KOH and CO$_2$ are between 0.05 and 0.35 wt. %. K. Xia et al. [25] studied CO$_2$ activation effect in ordered porous carbon CMK-3 applied in hydrogen storage. The H$_2$ adsorption of CMK-1 is around 1.2 wt.% at 1 bar and the activated carbons around 2 wt.%. Other routes to carbon structures with high volumetric capacity include templated carbon deposition on zeolites [26,27] and formation of activated carbon monoliths [28,29].

Metal particles dispersed in the porosity of active carbons are largely contributing to enhanced storage abilities. Although numerous studies focused on this feature, hydrogen spillover was generally evidenced. The catalyst is supposed to trigger H$_2$ dissociation; atomic hydrogen is then assumed to diffuse deeper in the microporous network and even between graphitic layers. Although platinum or palladium catalysts were shown to benefit from this mechanism, other studies evidenced such improvements by using cheaper metals [30]. Clearly, the hydrogen uptake capacity of carbon materials can be enhanced with the introduction of appropriate metal particles. Giraudet et al. [30] studied hydrogen adsorption on ordered MCs doped with nickel nanoparticles. Suryavanshi et al. [31] had incorporated ZnO nanoparticles inside the pore system of MC.

In this work, ordered porous carbon designated as CMK-1 was synthesized by replication from MCM-48 silica and then modified with metals and thermal treatments under different conditions in order to gain a higher hydrogen storage capacity.

Our goal was to evaluate the hydrogen storage capacities of CMK-1 replica modified with Zn and Ni nano species. The approach includes synthesis and characterization of carbon-modified nanostructures along with experimental study of their adsorption capacity and storage properties.

## 2. MATERIAL AND METHODS

### 2.1. Preparation of MCM-48 template

The mesoporous silicate was synthesized by hydrolysis of tetraethyl orthosilicate (TEOS, 98%, Sigma-Aldrich, Corp. St. Louis, MO, USA) at room temperature, in an aqueous solution, using cetyltrimethylammonium bromide (CTAB, Sigma-Aldrich) as a surfactant. The procedure designed is described as follows: Sodium hydroxide (NaOH, Sigma-Aldrich) and CTAB were dissolved in deionized water; TEOS was added to it. The molar composition of the gel was 1 M TEOS: 0.48 M NaOH: 0.48 M CTAB: 55 M H$_2$O. The solution was stirred for about 1 h and then transferred to a Teflon bottle and heated up to 373 K. After

3 days, the solution was cooled to room temperature, and its pH was adjusted by adding HCl. It was then heated at 373 K for 3 days. The product was filtered, washed, and dried in air at ambient temperature [32]. To remove the CTAB template, the sample was heated up from ambient temperature to 723 K under N$_2$ flow (20 mL/min) and subsequently calcined under air flow up to 723 K using a heating rate of 3 K/min [29].

## 2.2. Synthesis of CMK-1

Mesoporous carbons CMK-1 were prepared by carbonization of sucrose as carbon precursor. The procedure was the same as in our previous work on CMK-3 [33], except that the amounts of sucrose and sulfuric acid were modified according to the mesopore volume of MCM-48, 0.8 g sucrose, 0.1 g of H$_2$SO$_4$ in 3.0 g of deionized water per g of SiO$_2$. After being dried at 373 K for 5 h, this impregnation was repeated once again. The mixture was then dried at 433 K for 10 h, and the sucrose-MCM-48 composite was calcined at 1173 K during 5 h, under inert atmosphere (N$_2$, 25 mL/min) with the heating rate 4 K/min, to reach a complete carbonization. The pure carbonaceous product was obtained by dissolving the silica template hybrid composite with 3 wt. % HF at 298 K twice, to ensure complete dissolution of silicon. CMK materials were filtered, washed with water and ethanol, and dried. The sample was designated as CMK-1.

## 2.3. Synthesis of Zn-CMK-1

The samples were prepared by wetness impregnation using zinc nitrate (Sigma-Aldrich 98%, Zn(NO$_3$)$_2$·6H$_2$O) as source of Zn. A solution of zinc nitrate hexahydrate (Zn(NO$_3$)$_2$·6H$_2$O dissolved in ethanol) was mixed with carbon solution at ambient temperature, and the slurry was then kept for 24 h without stirring. The sample was afterwards dried at 373 K for 18 h. After that, the samples were desorbed in inert atmosphere from 298 to 473 K with a slope of 10 K/min and kept at this temperature during 5 h; temperature was then increased to 743 K with a slope of 10 K/min, kept at that temperature for 5 h. Nitrogen flow was always 20 mL/min. The sample was treated under H$_2$ flow at 773 K for 6 h with ramp rate 10 K/min. The sample was denoted as Zn-CMK-1. The percentage of Zn has been 5.5 wt.% before H$_2$ treatments and 5 wt.% with respect to carbon in the final Zn-CMK-1 material by inductively coupled plasma (ICP).

## 2.4. Synthesis of Ni-CMK-1

The samples were prepared by wetness impregnation using nickel(II) chloride hexahydrate (Sigma-Aldrich 98%, NiCl$_2$·6H$_2$O) as source of Ni (6 wt.%). Briefly, nickel nitrate was dissolved in ethanol, in which MC was mixed vigorously for 20 min. The sample was further dried under vacuum at 308 K until complete solvent evaporation. The powder obtained was dried at 353 K overnight. It was then transferred to a tube furnace exposed to nitrogen (20 mL/

min) at 773 K for 6 h and activated in a hydrogen flow at the same temperature for 6 h. The sample was denoted as Ni-CMK-1 according to ICP analysis with 5.5 wt.% of Ni species.

## 2.5. Characterization

Elemental analysis was performed by ICP atomic emission spectroscopy (Vista-MPX) operated with high-frequency emission power of 1.5 kW and plasma air flow of 12.0 L/min.

N$_2$ adsorption/desorption isotherms at 77 K were measured on ASAP 2020 equipment after degassing the samples at 673 K, determining textural properties as surface area and pore volume; pore size distribution was estimated using Barrett, Joyner, and Halenda algorithm. Hydrogen chemisorption characterization was performed in Micromeritics Chemisorb 2720 apparatus (Micromeritics Corporate Headquarters, USA), equipped with a thermal conductivity detector, at room temperature and atmospheric pressure. The samples were purged with N$_2$ (25 mL/min) at 673 K. The samples were cooled to 295 K and titrated with H$_2$ pulses in a stream of N$_2$ until a constant output thermal conductivity detector signal indicated saturation.

X-ray diffraction (XRD) patterns were recorded with a Philips X'Pert PRO PANalytical diffractometer (Westborough, MA, USA) under Cu K$\alpha$ radiation ($\lambda$ = 0.154 nm).

Fourier transform infrared spectroscopy studies were performed in a JASCO 5300 Fourier transform infrared spectrometer. KBr wafers were used to obtain Fourier transform infrared spectroscopy spectra for MCM-48, CMK-1, and metal-CMK-1 samples.

Scanning electron microscopy (SEM) micrographs were obtained by using a Nova NANOSEM 230 with energy-dispersive X-ray spectroscopy (EDS) (FEI Company, Oregon, USA). Samples were placed over an aluminum drum and covered with a gold film. The transmission electron microscopy (TEM) micrographs were taken on a TEM Philips EM 301 instrument, operated at 200 kV, and equipped with a field emission electron gun providing a point resolution of 0.17 nm evaluating Zn and Ni particle sizes.

X-ray photoelectron spectroscopy (XPS) spectra were obtained on a Microtech Multilb 3000 spectrometer, equipped with a hemispherical electron analyzer and MgK$\alpha$ (h$\nu$ = 1253.6 eV) photon source. An estimated error of ±0.1 eV can be assumed for all measurements. Intensities of the peaks were calculated from the respective peak areas after background subtraction and spectrum fitting by a combination of Gaussian/Lorentzian functions. The relative surface atomic ratios were determined from the corresponding peak intensities, corrected with tabulated sensitivity factors, with a precision of ±7%. Thermal studies (thermogravimetric analysis (TGA)) were carried out with a thermal analysis instrument (TA Instruments 2950 TGA differential scanning calorimetry, U.S. Microtech Inc. Head Quarters, Silicon Valley). The samples were exposed to a constant heating rate of 10 K/min from room temperature to 873 K, under

oxygen flow (10 mL/min). Hydrogen storage isotherms at 77 K at low and high pressure (up to 10 bars) were measured using an ASAP 2050 equipment appropriately calibrated. Before the hydrogen storage test, metal-doped carbons were heated under high vacuum at milder temperatures, 523 K for at least 8 h avoiding the possible decomposition of the metal nanoparticles at a higher temperature treatment. They were then cooled to room temperature. For the adsorption experiments, high-purity hydrogen gas (99.9999%) was used in the equipment. For the samples, hydrogen storage capacity was measured in a pressure range from 0 to 10 bars.

## 3. RESULTS AND DISCUSSION

### 3.1. X-ray diffraction, scanning electron microscope/transmission electron microscopy and Brunauer–Emmett–Teller studies

Figure 1 shows typical XRD patterns for the MCM-48 silica template and the carbon CMK-1 obtained following the aforementioned procedures. The low-angle XRD pattern of MCM-48 indicates excellent structural order for the cubic crystallographic space group Ia3d (Table I). However, the carbon CMK-1, obtained by removing the silica wall after carbonization, exhibits a different pattern relative to MCM-48. In contrast to CMK-2, 3, and 4, the structure of CMK-1 material, synthesized using silicate MCM-48 templates, was found to be not the exact negative replica of the template, because of a transformation of the mesostructure after the dissolution of the template wall. The main indication of structural transformation was the appearance on the XRD patterns of CMK-1 (Figure 1), of a strong low-angle diffraction peak (h·k·l·[1·1·0] at $2\theta = 1.67°$), not consistent with the symmetry of MCM-48 [20,33].
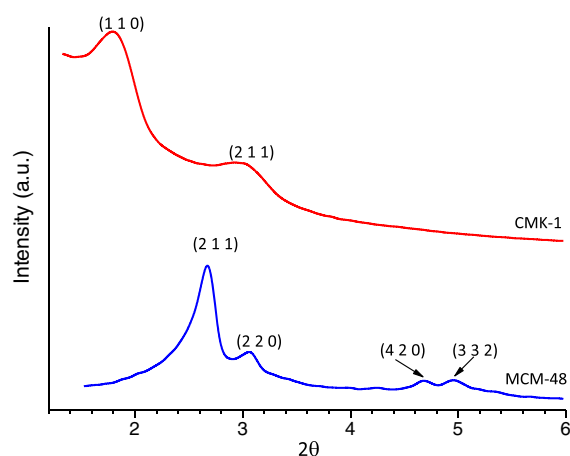


**Figure 1.** Small-angle X-ray diffraction patterns of MCM-48 and CMK-1.

As we can see in low-angle powder XRD pattern exists a structural transformation of the interwoven carbon framework after the dissolution of the silica wall. The subframeworks may be displaced with respect to one another to form contacts. Further transformation may as well involve a distortion of the frameworks. The main fact pointing to the structure transformation of the material is the appearance of a strong low-angle diffraction peak in the XRD powder pattern that is not consistent with the space group Ia3d of the MCM-48 template. This reflection is indexed as [1·1·0], and its emergence may be explained by lowering the material symmetry. The framework structure of CMK-1 is too complex to be described in such simple terms as 'pore', 'wall', or 'diameter' commonly used for describing the texture of mesoporous materials and molecular sieves. Nevertheless, it would be expedient to make an estimation of its geometric characteristics. The diameter of the roughly cylindrical framework segments may be determined, and these segments coincide with the Wyckoff symmetry positions 12c and 12d of the I4₁32 space group [34].

Figure 2 shows the low-angle XRD patterns of CMK-1 and the metal-modified samples. After the incorporation of the different metals, the overall pore structure is retained as indicated by the appearance of low-angle diffraction peaks (Table I). However, the peak intensity of the samples decreases greatly compared with that of the parent CMK-1. The loss in intensity is ascribed to the fact that the introduction of scattering material into the pores leads to an increased phase cancelation between scattering from the walls and the pore regions [35]. In the case of Zn-CMK-1 sample, the absence of XRD reflections can be attributed to a very high pore filling.
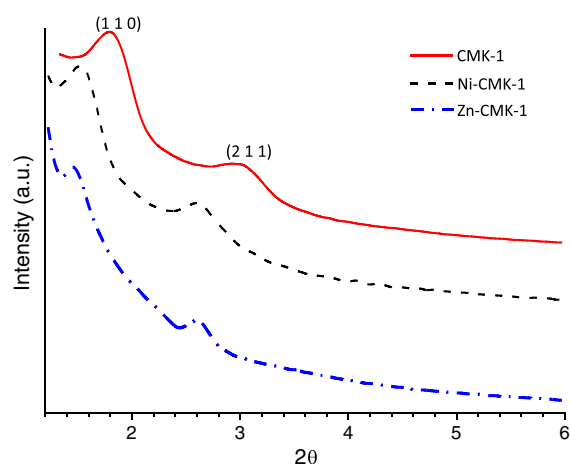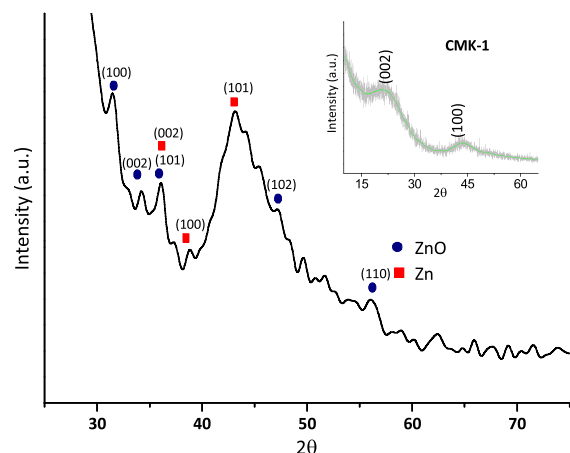
Figure 3 shows the wide-angle diffraction region of the sample modified with Zn (Zn-CMK-1). The inset XRD pattern at the wide-angle range (10–60°) of the CMK-1 host shows two broad diffraction peaks that can be indexed as [0·0·2] and [1·0·0] diffraction for typical graphite carbons [31].

The pattern of Zn-CMK-1 shows ZnO and metallic Zn signals [36,37] because the reduction process was probably not complete. The absence of prominent reflections in this pattern indicates that no crystalline bulk material has been formed outside the pore system, and the Zn/ZnO clusters are confined mostly inside the nanostructured carbon [38], showing nanometric size and high dispersion as seen in Table II and TEM studies.

The XRD pattern of Ni-CMK-1 (Figure 4) shows intensive peaks at $2\theta = 44.5°$, 51.8°, and 76.3°, corresponding to metallic Ni diffraction planes [1·1·1], [2·0·0], and [2·2·0], respectively [39]. The patterns are characteristic of a face-centered cubic lattice consisting of nickel nanoparticles. It may have NiO species, because the signals of NiO appeared very close to metallic Ni signals and would be overlapped [39] in the pattern, as will be shown later in TEM-EDS and XPS studies. While the nanomaterial area is significantly smaller with the incorporation of the metals, the characteristic structure of CMK-1 is maintained

**Table I.** X-ray diffraction parameters of samples.

| | MCM-48 (h·k·l) | | | | CMK-1 (h·k·l) | | |
| | 2·1·1 | 2·2·0 | 4·2·0 | 3·3·2 | 1·1·0 | 2·1·1 | |
| Sample | d (nm) | | | | d (nm) | | a$_o$ (nm) |
|---|---|---|---|---|---|---|---|
| Si-MCM-48 | 3.71 | 3.21 | 2.02 | 1.93 | — | — | 9.1 |
| CMK-1 | — | — | — | — | 5.85 | 3.35 | 8.2 |
| Zn-CMK-1 | — | — | — | — | 5.59 | — | 7.9 |
| Ni-CMK-1 | — | — | — | — | 5.78 | 3.32 | 8.2 |



**Figure 2.** Small-angle X-ray diffraction patterns of CMK-1, Ni-CMK-1, and Zn-CMK-1.



**Figure 3.** Wide-angle X-ray diffraction patterns of Zn-CMK-1 and CMK-1 (inset).

after the metal is within the host, in agreement with XRD studies (Table II).

Figure 5 shows the N$_2$ adsorption/desorption isotherms for MCM-48, CMK-1, Zn-CMK-1, and Ni-CMK-1 samples, and Table II displays the textural properties

determined from nitrogen physisorption analysis. The nitrogen adsorption–desorption isotherm for MCM-48 is a typical type IV curve, according to the International Union of Pure and Applied Chemistry (New Castle, DE, USA) classification, revealing the mesoporous nature of the material. The isotherm for CMK-1 and Zn-CMK-1 and Ni-CMK-1 samples exhibits hysteresis loops at a relative pressure range of 0.4–0.6, which can be attributed to capillary condensation–evaporation from the mesopores. It is clear that Zn-CMK-1 and Ni-CMK-1 reveal a reduced specific surface area (and a narrowed pore size), in comparison with those of pure MCM-48 and CMK-1 (Table II), with the corresponding incorporated metallic species.

The sharp peak at pore size distribution of CMK-1 and Zn and Ni-containing CMK-1 (Figure 6) indicates a fairly regular range of nanopores in carbonaceous materials, in correspondence with TEM observations.

Figure 7 shows SEM images of a clean CMK-1 without the inorganic template. MCM-48 still remains in the CMK-1 structure after the first hydrofluoric acid extraction; this fact is also proved by SEM-EDS (Figure S1 and S2)

Figure 8 shows TEM images of CMK-1. Ordered structure was shown to be slightly damaged by thermal treatments.

The TEM micrographs of Ni-CMK-1 and Zn-CMK-1 were depicted in Figure 9. The ordered cubic Ia3d mesostructure of metal-CMK-1 can be seen from Figure 9a and b, indicating that the ordered structure of CMK-1 is retained after the incorporation of Ni and Zn nanoparticles.

The places with darker contrast could be attributed to the presence of Zn and Ni particles with different dispersion. The small dark spots in the images could be ascribed to Zn and ZnO nanoparticles with average diameter of ~2.5 to 3 nm (Figure 9b), probably located into the host pores. The larger dark areas over the channels most likely correspond to NiO nanoparticle agglomerates on the external surface with average diameter of 11–13 nm (Figure 9a).

Energy-dispersive X-ray spectroscopy analysis was performed to determine the presence of Zn and Ni-containing CMK-1. The elemental compositions for C, O, and Zn and Ni nanoparticles were carefully evaluated (Figures 9c–d).

The maps collecting five spots indicate that the average of the atomic weight % of C, O, and Zn nanoclusters in Zn-CMK-1 is about 94.94%, 0.26%, and 4.80%, respectively. This result shows that only 20% of Zn species are as ZnO; whereas for Ni-CMK-1, it was 94.1%, 0.6%, and 5.3 wt.%

**Table II.** Textural and structural properties of the samples.

| Sample | Area m²/g | $V_P$ (cm³/g) mesoporous volume | BJH pore diameter (nm) | Metal cluster average size (nm)* | H₂ sorption (wt.%)** |
|---|---|---|---|---|---|
| Si-MCM-48 | 1034 | 0.96 | 2.22 | — | — |
| CMK-1 | 1089 | 0.69 | 3.11 | — | 2.1 |
| Zn-CMK-1 | 568 | 0.55 | 2.65 | Zn: 2.3 ZnO: 2.6 | 4.4 |
| Ni-CMK-1 | 560 | 0.51 | 2.50 | Ni + NiO: 12 | 2.4 |

BJH, Barrett, Joyner, and Halenda.
*Estimated by X-ray diffraction (Scherrer formula) and transmission electron microscopy.
**H₂ Sorption at 10 bars and 77 K.
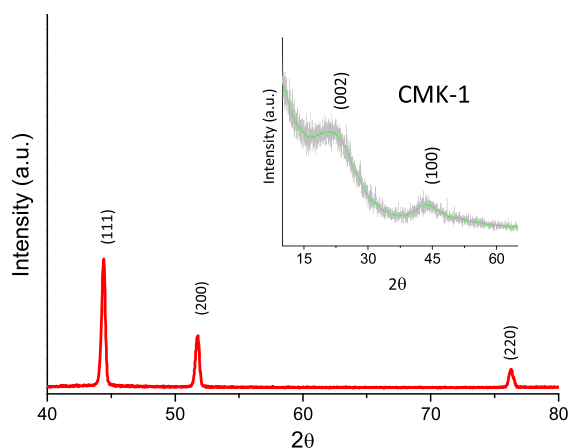


**Figure 4.** Wide-angle X-ray diffraction patterns of Ni-CMK-1 and CMK-1 (inset).

for C, O, and Ni, clearly indicating that the higher Ni content appears as oxide (about 40%).

### 3.1.1. Estimation of metallic cluster size by Scherrer formula

The XRD patterns analysis allows determining the crystal size of metallic particles in the samples and the effect obtained on metal dispersion. The average cluster size was estimated from the width of the diffraction peaks corresponding to different [h·k·l] Miller index using Scherrer formula [40] as we showed in the earlier work on CMK-3 [33].

For the application of Scherrer formula, we employed [1·0·1], [2·0·0], and [2·2·0] refraction planes for Ni-CMK-1. In the sample containing Zn species, [1·0·0] and [1·0·1] for Zn⁰ and [1·0·0], [0·0·2], and [1·1·0] for ZnO diffraction planes were used.

The average diameters of metal particles obtained by Scherrer formula were 13 nm for Ni-CMK-1 and 2.3 and 2.6 nm for metallic Zn and ZnO in Zn-CMK-1, respectively.

### 3.2. Infrared spectroscopy analysis

Fourier transform infrared spectroscopy spectra show characteristic bands of MCM-48 that indicate great crystallinity of material (Figure S3). The peak at around $1638 \, cm^{-1}$

corresponds to the bending mode of O–H of water. The peaks around 1288 and $1180 \, cm^{-1}$ are attributed to the asymmetric stretching of Si–O–Si groups. The band at $806 \, cm^{-1}$ and a broad signal appears at $580 \, cm^{-1}$ is assigned to the symmetric stretching modes of Si–O–Si groups. The peak at $963–967 \, cm^{-1}$ is attributed to the presence of defective Si–OH groups while the adsorption band at $458 \, cm^{-1}$ is due to Si–O–Si bending vibration. In carbon CMK-1 and metal/CMK-1, these bands disappeared because the siliceous material was eliminated in the process of carbon synthesis.

### 3.3. X-ray photoelectron spectroscopy characterization

X-ray photoelectron spectroscopy data of Zn-CMK-1 showed that zinc is as $Zn^0$ or $Zn^{2+}$ ions (Figure 10), according to the binding energies (BEs) of $Zn2p_{3/2}$ electron at 1022.5 eV. The Zn $2p_{3/2}$ spectrum of Zn oxide, although free from multiplet splitting and other complex effects, suffers from an overlap with $Zn^0$ species peak BE [41]. According to Woll [42], the Zn $2p_{3/2}$ lines for Zn and ZnO are quoted at 1021.4 and 1021.7 eV, respectively.

The split 2p electron energy levels $Ni(2p_{3/2})$ and $Ni(2p_{1/2})$ appeared at 850–865 eV and 865–885 eV, respectively (Figure 11). These bond energies are higher here by 1.5–2.0 eV compared with those of the pure NiO [43]. This deviation is probably ascribed to the difference in coordination of $Ni^{2+}$ on CMK-1 and in NiO. It is highly probable that $Ni^{2+}$ ions are coordinated in higher symmetry in CMK-1, possessing a well-ordered crystal structure compared with that in NiO. The satellite band appearing at higher bond energy values also supports the typical oxide structure.

Activation under H₂ leads to a partial reduction of the surface $Ni^{2+}$ species forming $Ni^0$ (reduced catalyst). The reactive surface contains, in addition to $Ni^0$, mixed $Ni^0 + NiO$. The mixed nickel compounds (e.g., nickel oxides and hydroxides) can be present in relatively large particles, where the NiO compound can be localized on the outer surface, and metallic Ni exists in a subsurface region near the support, respectively. This behavior can be explained by the drastic changes of the electronic structure of the deposits as the cluster size increases. The size of
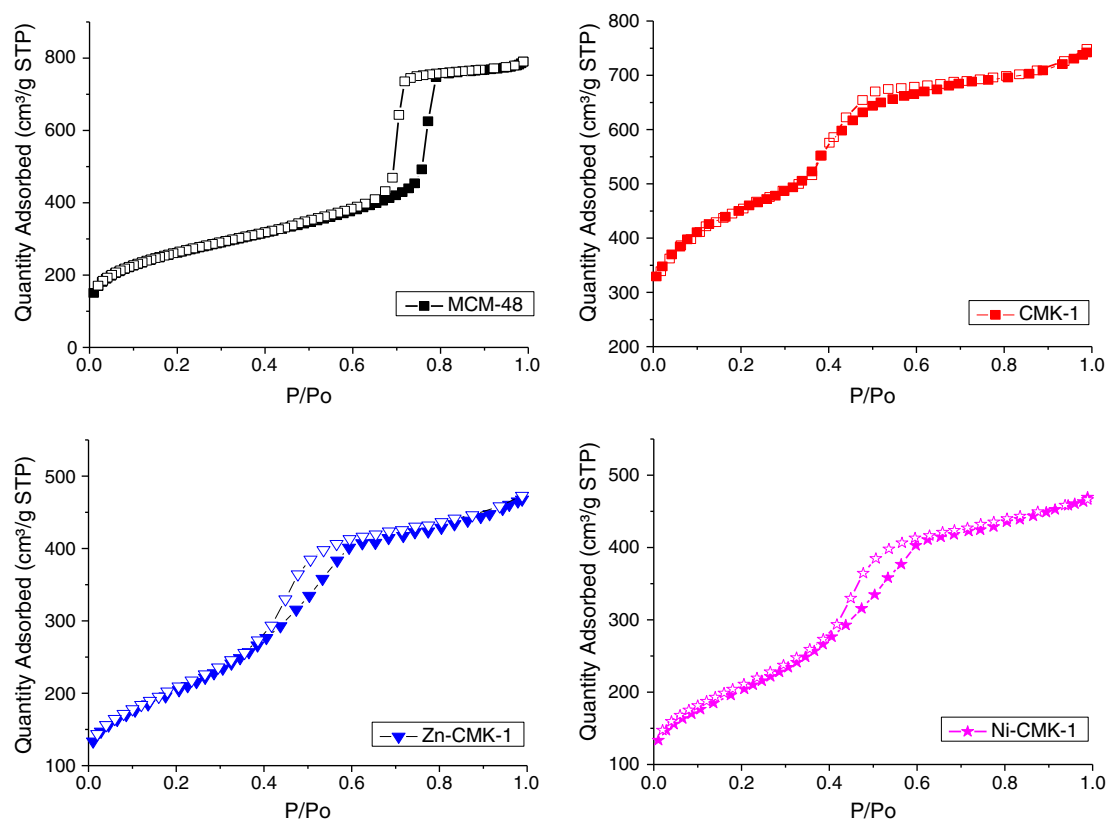
**Figure 5.** N$_2$ adsorption–desorption isotherms of MCM-48, mesoporous carbon CMK-1, Zn-CMK-1, and Ni-CMK-1.
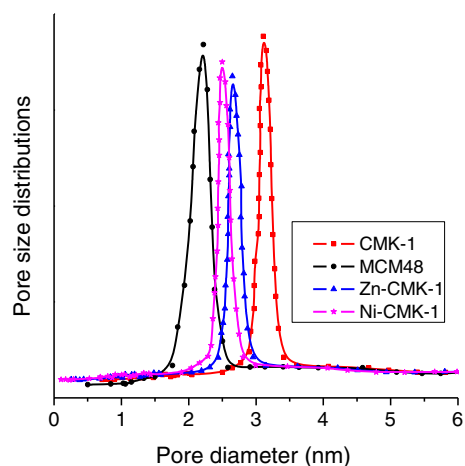


**Figure 6.** Pore size distribution of MCM-48, CMK-1, Zn-CMK-1, and Ni-CMK-1.

the cluster determines the final state in the photoemission process because, after the photoemission, the positive charge left on the aggregate can be less screened delocalized, when compared with an extended metallic system. This results in a shift of the XPS spectrum corresponding to the Coulomb energy of localized charge. It was found that the shift is proportional to the reciprocal

particle diameter [44]. Consequently, the BEs of small metal aggregates should be found at higher values as indeed observed in many cases. According to elemental XPS analysis (C1s, O1s, and Zn 2p$_{3/2}$), the chemical composition (% at.) of Zn-CMK-1 for C, O, and Zn at 5-10 nm of depth was 99.64%, 0.16%, and 0.2%, respectively. However, using EDS analysis (Figure 9c–d), the nominal Zn was 4.85 wt.% suggesting that most Zn$^0$ (74% Zn atoms) is within the nanostructure of CMK-1 sample. Moreover, O concentration by XPS was about 80% of total oxygen atom, supporting the idea that ZnO nanoclusters are on the external surface of Zn-CMK-1 material.

Unlike what was found in the case of Zn-CMK-1, the XPS results of Ni-CMK-1 indicate a distribution of C, O, and Ni, 99 0.375 and 0.625 atoms %, compared with the EDS results (0.6% and 5.3 wt.% for O and Ni, respectively). Thus, a great proportion of nickel is on the outer surface (>40%) as NiO, corresponding to lower amount of reduced Ni species found in Ni-CMK-1 nanostructured material. The results of EDS and XPS for Zn and Ni support the difference of the cluster size obtained by XRD (Scherrer formula) and TEM, shown in Table I and Figure 9 (2.5 and 12 nm, respectively). This indicates that CMK-1 nanostructure prevents the growth of large crystals in its nanopores, particularly during the incorporation of zinc.

Thermogravimetric analysis (not shown) has been recorded in air for CMK-1 samples: 5 wt.% of Zn
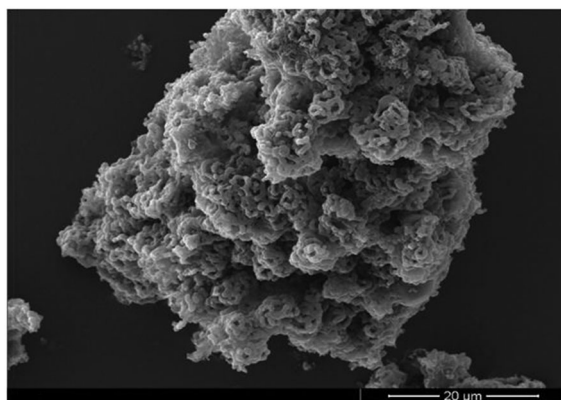
**Figure 7.** Scanning electron microscope images of CMK-1.

(Zn-CMK-1) and 5.5 wt.% of Ni (Ni-CMK-1) impregnated CMK-1 hosts, from 373 to 800 K.

For CMK-1, composed of amorphous carbon, the combustion was initiated before 373 K. A linear weight loss has been observed for CMK-1 (with 80% weight loss from 373 to 800 K), because a structure with plenty of pores facilitates air diffusion in order to burn carbon into CO and CO$_2$ products. As the Zn species has been impregnated inside CMK-1, a lower weight loss can be seen around 630 K, with 68% weight loss after this temperature; whereas for CMK-1, weight loss amounted to 80%. That means that Zn$^0$ and ZnO nanoparticles inside CMK-1 also prevent the collapsing of CMK-1 framework by increasing the decomposition temperature. The final weight loss at 773 K for Zn-CMK-1 was 94.5%, close to the expected value of the Zn species in CMK-1 sample after H$_2$ reduction (5 wt.%). For Ni-CMK-1 sample, a similar behavior can be observed by reaching 95% of weight loss at 800 K. Because of confinement of uniform pore structure, most trapped nanoparticles of Zn and Ni could keep their uniformity even at high temperatures.

### 3.4. Hydrogen uptake measurements

The capacity of hydrogen storage was evaluated at low and high pressures and cryogenic temperatures (77 K).

The experimental data were fitted by Freundlich isotherm [45], that is, a purely empirical formula for gaseous adsorbates. The Freundlich model is described by the following equation:

$$Q = K_F P^{\frac{1}{n}}$$

where $Q$ is the quantity adsorbed per unit mass of adsorbent, $P$ is the pressure of adsorbate, and $K_F$ and $n$ are empirical constants, called Freundlich constants, for each adsorbent–adsorbate pair at a given temperature. The $K_F$ is a measurement of the adsorption, and $n$ is a measure of the adsorption intensity [45]. The experimental data were fitted to this equation using nonlinear least square regression for arbitrary fit functions and minimizing the objective function by employing Levenberg–Marquardt method. The fitting accuracy was $R^2 = 0.97$.

Figure 12 shows the isotherms of hydrogen at 77 K on the different materials studied at a range of pressures (0–10 bars). The inset of this figure shows the behavior at low pressures (0–1 bar).

Zn-CMK-1 sample has the highest hydrogen uptake (0–10 bars) (Table II). At lower pressures (0–0.3 bar), hydrogen uptake of Ni sample is slightly lower than that of CMK-1, yet at high pressures, the sample with Ni shows greater H$_2$ adsorption than CMK-1.

We refer to storage as 'uptake' (carbon like a sponge); thus, the process is completely reversible, and the curve becomes in same place, because every point returns to initial values when measurements were carried out without liquid nitrogen pressure. The treatment under hydrogen flow at moderately high temperatures is for attempt to reduce the oxide cluster to a metallic cluster because the electronic configuration of metal cluster is better to interact with hydrogen molecules and for high H$_2$ storage.

The experimental data obtained of hydrogen storage on nonactivated (before hydrogen treatment), for Zn-CMK-1 and Ni-CMK-1 materials (Figure S4), indicate that the hydrogen storage of nonactivated are lower than activated materials. Hence, we try to achieve a more hydrogen uptake on metallic clusters.
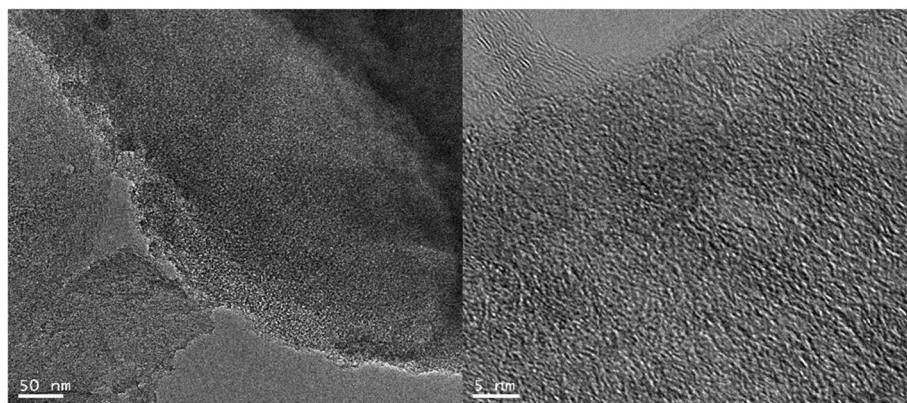


**Figure 8.** Transmission electron microscopy images of CMK-1.
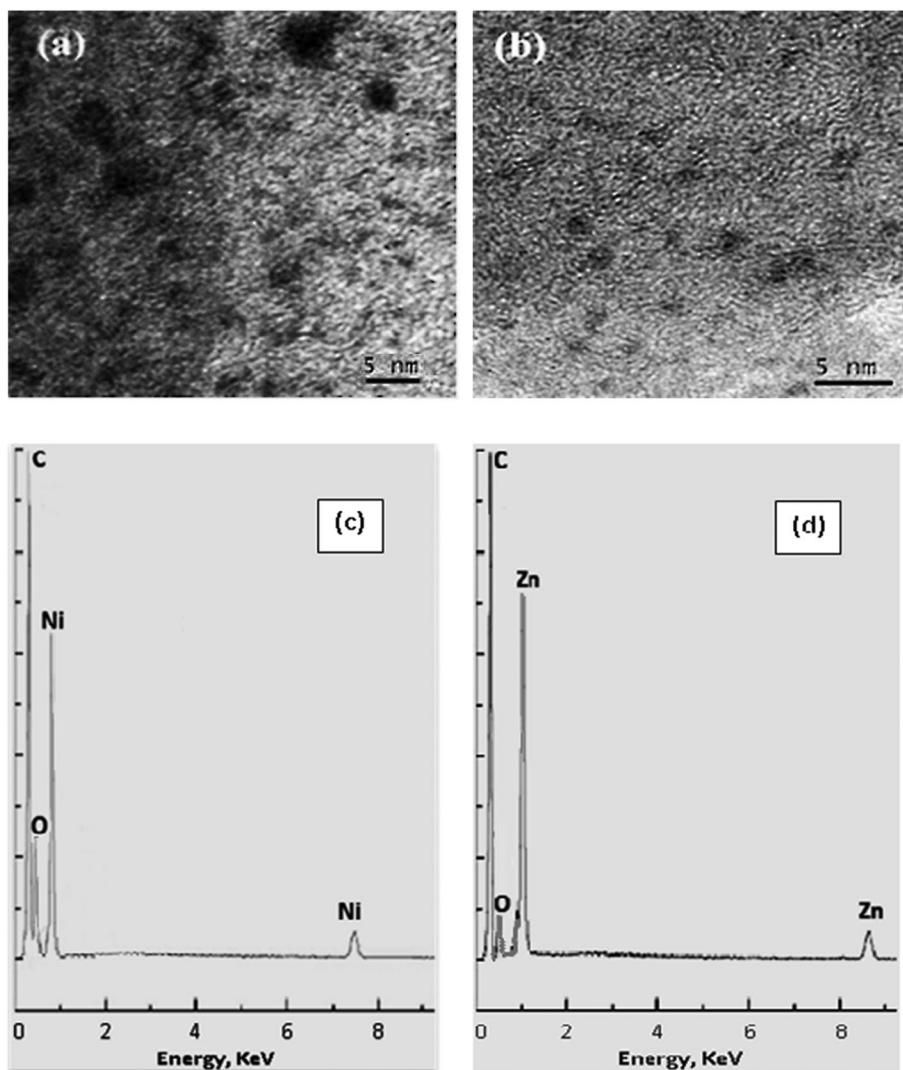
**Figure 9.** Transmission electron microscopy images of (a) Ni-CMK-1 and (b) Zn-CMK-1; energy-dispersive X-ray spectroscopy spectrum of (c) Ni-CMK-1 and (d) Zn-CMK-1.

Figure 13 shows the mechanism proposed for hydrogen storage in CMK-1 modified with metals in agreement with Kim *et al.* [13].

There are at least two ways in the process of hydrogen physisorption on metal-CMK-1 surface. Hydrogen molecules spill over onto the CMK-1 nano/micropores and are adsorbed onto nanometric metal clusters. Hydrogen adsorption was found to be fully reversible, indicating that there was no chemical reaction or strong bond between hydrogen and metal nanocluster or CMK-1 framework.

Therefore/hence, a dipole-induced model is proposed. The first layer of hydrogen molecules could react with the metal cluster because of the high oxidation capacity of metals interacting as dihydrogen complex [46], yet the amount of this initial interaction is particularly negligible. The second layer of hydrogen molecules is physically adsorbed by dipole-induced interaction. Hydrogen molecules are basically nonpolar, but the strong interaction of

metal particles leads to the dipole-induced effects on hydrogen molecules. The third layer and any upper layer of hydrogen molecules could interact with metal cluster by this mechanism; however, the force of the dipole-induced bond is weak and decreases when distance to the surface increases. This mechanism can be thus applied at higher pressures; at a higher pressure, metal-CMK-1 adsorbs more amount of hydrogen than does carbon.

Hydrogen pulse chemisorption was carried out in the samples. In all samples, hydrogen chemisorption at room temperature was negligible (CMK-1 does not show H$_2$ chemisorption, Zn-CMK-1: 0.0746 mL/g and Ni-CMK-1: 0.0032 mL/g), indicating that there was no chemical reaction or strong H$_2$-metal bond, and that hydrogen adsorption was fully reversible.

Theoretically, the 3D states of metals mainly contributed to ground-state electronic structure near the Fermi level of metal-CMK-1 and, to some degree, the *p* states
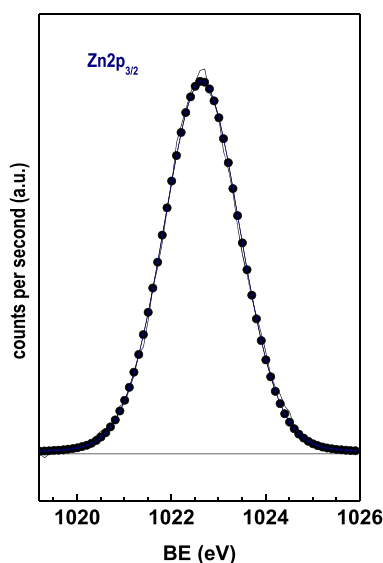
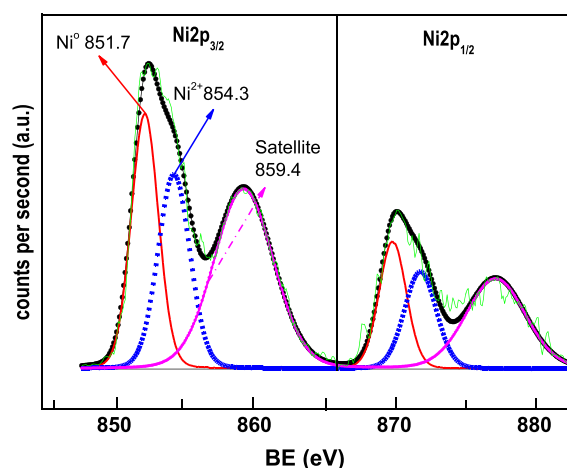**Figure 10.** Zn-CMK-1 X-ray photoelectron spectroscopy spectrum.



**Figure 12.** Hydrogen isotherm sorption curves of: (A) CMK-1, Zn-CMK-1, and Ni-CMK-1; (B) CMK-1 and ZnO-CMK-1; and (C) NiO-CMK-1 at 77 K.



**Figure 11.** X-ray photoelectron spectroscopy binding energies spectra of the Ni 2p$_{3/2}$ and Ni 2p$_{1/2}$ peak region separated by a vertical line. Gaussian component: Ni$^0$ solid line; NiO dot line, and satellite peak of NiO dash dot line.



**Figure 13.** Scheme for the proposed mechanism of metal-CMK-1 and hydrogen interaction.

of carbon. Those contributions of 3D states decrease as we move across the periodic table from Mn to Zn following the increase of d orbital occupancies [47]. Hydrogen bonds to the metal results in an opening of highest occupied molecular orbital–lowest unoccupied molecular orbital energy gap in case of Ni-CMK-1. While it shows a reduction in HOMO-LUMO energy gap for Zn-CMK-1 resulting in an appearance of molecular electronic states that allow a better H$_2$ physisorption.

Moreover, the 'spillover' mechanism by which metal nanoparticles help make it possible to store hydrogen in carbon matrix. The atomic-scale understanding of the hydrogen spillover mechanism for hydrogen storage in metal-doped carbon materials and metal–organic frameworks is discussed
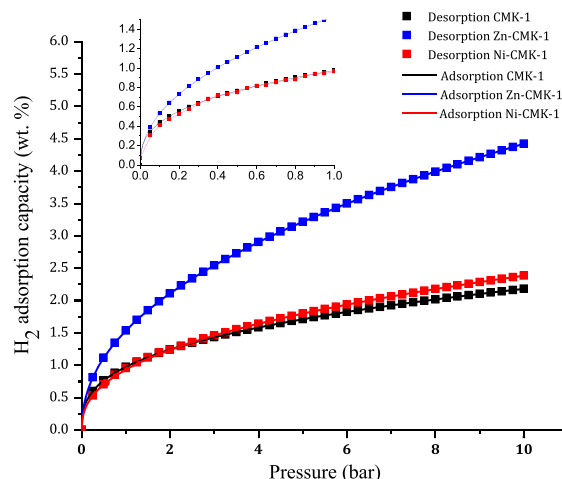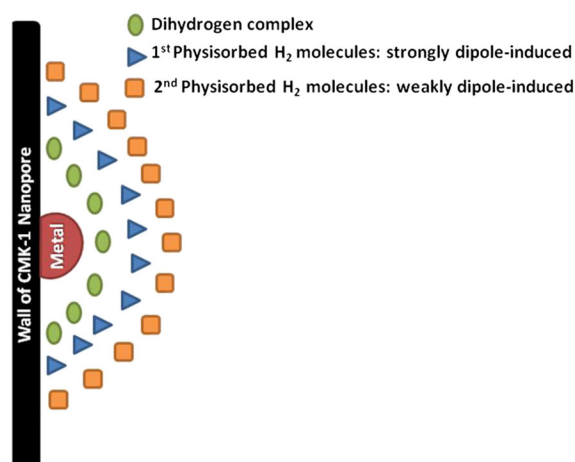
by critically assessing recent computational and experimental studies. It is argued that the spillover mechanism involves the following: (i) the generation and desorption of mobile H atoms on the metal nanoparticles; (ii) the diffusion of H atoms in weakly bound states on the support; (iii) the sticking and immobilization of H atoms at preferential locations of the receptor where barriers to sticking are decreased; and (iv) the Eley–Rideal recombination of the adsorbed H atoms with diffusing mobile H atoms to form H$_2$ [48].

# 4. CONCLUSIONS

Promising hydrogen storage materials can be obtained from ordered porous carbon CMK-1 modified with Ni

and Zn, which was synthesized by replication using MCM-48 as template. The incorporation of metals was carried out by wetness impregnation considering both the effects of thermal treatments employing H$_2$.

Nanoparticles of Zn ($>70\%$ as Zn$^0$) in Zn-CMK-1 have a smaller size than those of Ni (mostly NiO with 12 nm average size). Consequently, metal dispersion is higher, and the occlusion of nanopores of the carbon framework is lower than that of Ni-CMK-1. The enhanced activity and performance of Zn-CMK-1 derives from improved dispersion of Zn nanoparticles and a better use of the support, probably causing a high metal surface area. This indicates the better hydrogen adsorption of Zn-CMK-1 sample. However, at high pressures, Ni-CMK-1 adsorbs more amount of hydrogen than carbon because H$_2$/metal or H$_2$/metal oxide interactions become more evident. A hydrogen storage mechanism on metal/carbon surfaces was proposed. We can conclude by indicating that CMK-1 hydrogen storage capacity was increased by addition of metal clusters. Moreover, hydrogen storage behaviors onto Zn-CMK-1 and Ni-CMK-1 can be optimized by controlling the metal cluster size and dispersion and by increasing the carbon specific surface area.

## ACKNOWLEDGEMENTS

## REFERENCES

1. Cho SJ, Choo K, Kim DP, Kim JW. H$_2$ sorption in HCl-treated polyaniline and polypyrrole. *Catalysis Today* 2007; **120**:336–340.

2. White CM, Steeper RR, Lutz AE. The hydrogen-fueled internal combustion engine: a technical review. *International Journal of Hydrogen Energy* 2006; **31**(10):1292–1305.

3. Jurczyk MU, Kumar A, Srinivasan S, Stefanakos E. Polyaniline-based nanocomposite materials for hydrogen storage. *International Journal of Hydrogen Energy* 2007; **32**(1):1010–1015.

4. Schlapbach L, Züttel A. Hydrogen-storage materials for mobile applications. *Nature* 2001; **414**:353–358.

5. Kajiura H, Tsutsui S, Kadono K, Kakuta M, Ata M, Murakami Y. Hydrogen storage capacity of commercially available carbon materials at room temperature. *Applied Physics Letters* 2003; **82**:1105–1107.

6. Mandoki NT, Dentzer J, Piquero T, Saadallah S, David P, Guterl CV. Hydrogen storage in activated carbon materials: role of the nanoporous texture. *Carbon* 2004; **42**:2744–2747.

7. Züttel A, Sudan P, Mauron P, Kiyobayashi T, Emmenegger C, Schlapbach L. Hydrogen storage in carbon nanostructures. *International Journal of Hydrogen Energy* 2002; **27**:203–212.

8. Musyoka NM, Ren J, Langmi HW, Rogers DEC, North BC, Mathe M, Bessarabov D. Synthesis of templated carbons starting from clay and clay-derived zeolites for hydrogen storage applications. *International Journal of Energy Research* 2014. doi:10.1002/er.3261.

9. Klyamkin SN, Chuvikov SV, Maletskaya NV, Kogan EV, Fedin VP, Kovalenko KA, Dybtsev DN. High-pressure hydrogen storage on modified MIL-101 metal–organic framework. *International Journal of Energy Research* 2014; **38**:1562–1570.

10. Ren J, Langmi HW, North BC, Mathe M. Review on processing of metal–organic framework (MOF) materials towards system integration for hydrogen storage. *International Journal of Energy Research* 2014. doi:10.1002/er.3255.

11. Singer JP, Mayergoyz A, Portet C, Schneider E, Gogotsi Y, Fischer JE. Enhanced volumetric hydrogen storage capacity of porous carbon powders by forming peels or pellets. *Microporous ann M esoporous Materials* 2008; **116**:469–472.

12. Poirier E, Chahine R, Bose TK. Hydrogen adsorption in carbon nanostructures. *International Journal of Hydrogen Energy* 2001; **26**:831–835.

13. Kim BJ, Park SJ. Optimization of the pore structure of nickel/graphite hybrid materials for hydrogen storage. *International Journal of Hydrogen Energy* 2011; **36**:648–653.

14. Ströbel R, Garche J, Moseley PT, Jörissen L, Wolf G. Hydrogen storage by carbon materials. *Journal of Power Sources* 2006; **159**(2):781–801.

15. Yang H, Zhao D. Synthesis of replica mesostructures by nanocasting strategy. *Journal of Material Chemistry* 2005; **15**:1217–1231.

16. Gadiou R, Saadallah SE, Piquero T, David P, Parmentier J, Guterl CV. The influence of textural properties on the adsorption of hydrogen on ordered nanostructured carbons. *Microporous and Mesoporous Materials* 2005; **79**:121–128.

17. Fang BZ, Zhou HS, Honma I. Ordered porous carbon with tailored pore size for electrochemical hydrogen storage application. *Journal of Physical Chemistry B* 2006; **110**:4875–4880.

18. Guterl CV, Frackowiak E, Jurewicz K, Friebe M, Parmentier J, Béguin F. Electrochemical energy

storage in ordered porous carbon materials. *Carbon* 2005; **43**:1293–1302.

19. Yang ZX, Xia YD, Sun XZ, Mokaya R. Preparation and hydrogen storage properties of zeolite-templated carbon materials nanocast via chemical vapor deposition: effect of the zeolite template and nitrogen doping. *Journal of Physical Chemistry B* 2006; **110**:18424–18431.

20. Ryoo R, Joo SH, Jun S. Synthesis of highly ordered carbon molecular sieves via template-mediated structural transformation. *Journal of Physical Chemistry B* 1999; **103**:7743–7746.

21. Joo SH, Jun S, Ryoo R. Synthesis of ordered mesoporous carbon molecular sieves CMK-1. *Microporous ann Mesoporous Materials* 2001; **44–45**:153–158.

22. Jun S, Joo SH, Ryoo R, Kruk M, Jaronice M, Liu Z, *et al.* Synthesis of new, nanoporous carbon with hexagonally ordered mesostructure. *Journal of American Chemical Society* 2000; **122**:10712–10713.

23. Smith MR, Bittner EW, Shi W, Johnson JK, Bockrath BC. Chemical activation of single-walled carbon nanotubes for hydrogen adsorption. *Journal of Physical Chemistry B* 2003; **107**:3752–6370.

24. Blackman JM, Patrick JW, Arenillas A, Shi W, Snape CE. Activation of carbon nanofibres for hydrogen storage. *Carbon* 2006; **44**:1376–1385.

25. Xia K, Gao Q, Wu C, Song S, Ruan M. Activation, characterization and hydrogen storage properties of the mesoporous carbon CMK-3. *Carbon* 2007; **45**:1989–1996.

26. Yang Z, Xia Y, Mokaya R. Enhanced hydrogen storage capacity of high surface area zeolite-like carbon materials. *Journal of the American Chemical Society* 2007; **129**:1673–1679.

27. Hou P-X, Orikasa H, Itoi H, Nishihara H, Kyotani T. Densification of ordered microporous carbons and controlling their micropore size by hot-pressing. *Carbon* 2007; **45**:2011–2016.

28. Lozano-Castelló D, Cazorla-Amorós D, Linares-Solano A, Quinn DF. Activated carbon monoliths for methane storage: influence of binder. *Carbon* 2002; **40**:2817–2825.

29. Jorda-Beneyto M, Lozano-Castello D, Suarez-Garcia F, Cazorla-Amoros D, Linares-Solano A. Advanced activated carbon monoliths and activated carbons for hydrogen storage. *Microporous and Mesoporous Materials* 2008; **112**:235–242.

30. Giraudet S, Zhu Z. Hydrogen adsorption in nitrogen enriched ordered mesoporous carbons doped with nickel nanoparticles. *Carbon* 2011; **49**:398–405.

31. Suryavanshi U, Iijima T, Hayashia A, Hayashi Y, Tanemura M. Fabrication of ZnO nanoparticles confined in the channels of mesoporous carbon. *Chemical Engineering Journal* 2012; **179**:388–393.

32. Wang S, Wu D, Sun Y, Zhong B. The synthesis of MCM-48 with high yields. *Materials Research Bulletin* 2001; **36**(9):1717–1720.

33. Juarez J, Gomez MB, Anunziata OA. Synthesis and characterization of Pt-CMK-3 hybrid nanocomposite for hydrogen storage. *International Journal of Energy Research* 2014 in press. DOI: 10.1002/er.3229.

34. Solovyov LA, Zaikovskii VI, Shmakov AN, Belousov OV, Ryoo R. Framework characterization of mesostructured carbon CMK-1 by X-ray powder diffraction and electron microscopy. *Journal of Physical Chemistry B* 2002; **106**:12198–12202.

35. Huwe H, Fröba M. Iron (III) oxide nanoparticles within the pore system of mesoporous carbon CMK-1: intra-pore synthesis and characterization. *Microporous and Mesoporous Materials* 2003; **60**:151–158.

36. Ning G-H, Zhao X-P, Li J, Zhang C-Q. Hugely enhanced electroluminescence from mesoporous ZnO particles. *Optical Materials* 2006; **28**:385–390.

37. Chen R, Han J, Yan X, Zou C, Bian J, Alyamani A, Gao W. Photocatalytic activities of wet oxidation synthesized ZnO and ZnO-TiO$_2$ thick porous films. *Applied Nanoscience* 2011; **1**:37–44.

38. Gómez Costa MB, Juárez JM, Martínez ML, Beltramone AR, Cussa J, Anunziata OA. Synthesis and characterization of conducting polypyrrole/SBA-3 and polypyrrole/Na-AlSBA-3 composites. *Material Research Bulletin* 2013; **48**:661–667.

39. Veena Gopalan E, Malini KA, Santhoshkumar G, Narayanan TN, Joy PA, Al-Omari IA, Sakthi Kumar D, Yoshida Y, Anantharaman MR. Template-assisted synthesis and characterization of passivated nickel nanoparticles. *Nanoscale Research Letters* 2010; **5**:889–897.

40. Langford JI, Wilson AJC. Scherrer after sixty years: A survey and some new results in the determination of crystallite size. *Journal of Applied Crystallography* 1978; **11**:102–113.

41. Biesinger MC, Lau LWM, Gerson AR, Smart RSC. Resolving surface chemical states in XPS analysis of first row transition metals, oxides and hydroxides: Sc, Ti, V, Cu and Zn. *Applied Surface Science* 2010; **257**:887–898.

42. Wöll C. The chemistry and physics of zinc oxide surfaces. *Progress in Surface Science* 2007; **82**:55.

43. Kónya Z, Vesselényi I, Kiss J, Farkas A, Oszkó A, Kiricsi I. XPS study of multiwall carbon nanotube synthesis on Ni-, V-, and Ni, V-ZSM-5 catalysts. *Applied Catalysis, A: General* 2004; **260**(1):55–61.

44. Loviat F, Czekaj I, Wambach J, Wokaun A. Nickel deposition on γ-Al$_2$O$_3$ model catalysts: an experimental

and theoretical investigation. *Surface Science* 2009; **603**(14):2210–2217.

45. Zeinaldi F, Ghoreyshi AA, Najafpour GD. Adsorption of dichloromethane from aqueous phase using granular activated carbon: isotherm and breakthrough curve measurements. *Middle East Journal science Research* 2010; **5**(4):191–198.

46. Kubas GJ. Metal dihydrogen and $\sigma$-bond complexes: structure, theory, and reactivity. 1st ed. Springer; 2001. ISBN 0-306-46465-9.

47. Nguyen TQ, Bustria Padama AA, Sison Escano MC, Kasai H. Theoretical study on the adsorption of NO on metal macrocycles, metal = Mn,Fe,Co,Ni,Cu,Zn. *ECS Transactions* 2013; **45**(20):91–100.

48. Psofogiannakisa GM, Froudakis GE. Fundamental studies and perceptions on the spillover mechanism for hydrogen storage. *Chemical Communications* 2011; **47**:7933–7943.

## SUPPORTING INFORMATION

Additional supporting information may be found in the online version of this article at the publisher's web site.